RSC Advances

PAPER

View Article Online
View Journal | View Issue

Cite this: *RSC Adv.*, 2026, **16**, 12141

Development of a bimetallic Cu/Mg/MCM catalyst for glycerol hydrogenolysis to propanediol without external hydrogen

Anita Ramli *[a] and Nur Akila Syakida Idayu Khairul Anuar[b]

The catalytic performance of all monometallic and bimetallic catalysts for the hydrogenolysis of glycerol to 1,2-propanediol (1,2-PDO) and 1,3-propanediol (1,3-PDO) was evaluated in a high-pressure batch reactor operated at 180–220 °C for 1–4 hours under 5 bar (1,2-PDO) and 20 bar (1,3-PDO) of N_2 using various solvents as *in situ* hydrogen sources with different catalyst loading (0.1–0.5 g). Commercial Al-MCM-41 was impregnated with different contents of monometallic Cu and different ratios of Cu/Mg/MCM *via* the incipient wetness impregnation technique, followed by drying at 100 °C for 24 hours and calcination at 550 °C for 5 hours. The catalysts' physicochemical properties were analyzed using XRD, N_2 adsorption–desorption isotherms, and H_2-TPR. The XRD patterns of all the synthesized catalysts revealed diffraction peaks corresponding to a well-ordered two-dimensional hexagonal structure of the MCM support at low angles, along with the presence of CuO and MgO phases at higher angles. A progressive decrease in the surface area and pore volume was observed with increasing the Cu and Mg loading. The association of Cu with Mg in a synergistic interaction resulted in decreasing the reduction temperature, proving the occurrence of the MgO hydrogen spillover effect as the Cu content was greater than that of Mg. The performance of all catalysts was assessed in glycerol hydrogenolysis reactions without the addition of external hydrogen gas to investigate the influence of Cu/Mg loading on the MCM-supported catalyst efficiency for the production of 1,2-PDO and 1,3-PDO.

Received 3rd August 2025
Accepted 27th January 2026

DOI: 10.1039/d5ra05648a

rsc.li/rsc-advances

Introduction

The concerns over the global warming and energy security have caused major progress in the field of alternative sources of renewable energy as the cleaner substitutes of liquid fuels and chemicals produced from petroleum. One of these renewable, environmentally friendly fuels derived from biomass that may immediately replace conventional petroleum diesel is biodiesel. The rapid expansion of the biodiesel industries has generated an abundant supply of crude glycerol, turning this once valuable byproduct into surplus waste material due to its excessive availability.[1] Glycerol is the main byproduct that is generated during biodiesel production. Nevertheless, the increase in the production of glycerol from biodiesel refining, accompanied with the tight markets of glycerol supply and demand, has created a glut in the glycerol market. This resulting glut has driven glycerol price down and left biodiesel refiners with limited options for managing this byproduct.[2]

Over the past decades, the hydrogenolysis of higher polyols like sorbitol, xylitol, and glycerol into value-added chemicals has emerged as an attractive process for glycerol valorization.[3,4] One of the glycerol valorization strategies that has received much attention is the catalytic transfer hydrogenolysis reaction that mainly produces 1,2- and 1,3-propanediols (1,2-PDO and 1,3-PDO) and uses renewable H-donors in liquid media.[5] This approach is considered one of the most economically and environmentally beneficial techniques to substitute the conventional hydrodeoxygenation processes (CHDO).[6] Currently, 1,2-PDO derived from the hydrogenolysis of glycerol is employed in the production of unsaturated polyester resins and antifreeze or deicing fluids,[7] while the primary use of 1,3-PDO is the production of highly valuable polyester fibers, films, coatings and engineering plastics.[8] In this study, the catalytic transfer hydrogenolysis of glycerol was performed on different catalysts/support combinations to explore their influence on product selectivity and efficiency.[9]

Zeolite is widely used as a catalyst support due to its high surface area, and its acidic nature favors the formation of acetol as an intermediate in glycerol hydrogenolysis.[10] However, the acidity of the zeolite as a solid acid might affect the catalyst's activity and modulate the over-hydrogenolysis. This would lead to more gaseous or lower carbon compounds such as ethylene glycol, ethanol, methanol, methane, CO_2 and H_2 formation,

[a]*HICoE Centre of Biofuel and Biochemical Research, Institute of Sustainable Energy & Resources (ISER), Universiti Teknologi PETRONAS, Seri Iskandar 32610, Perak, Malaysia. E-mail: anita_ramli@utp.edu.my*

[b]*Fundamental and Applied Sciences Department, Universiti Teknologi PETRONAS, Seri Iskandar 32610, Perak, Malaysia. E-mail: nurakila.khairul@utp.edu.my*

mainly due to excessive cleavage of the C–C bond rather than C–O bonds.[11] It was revealed that the strong acid sites in the HZSM-5-based catalyst converted glycerol into gaseous products (mainly CH_4) and ethylene as the acidity of the catalyst increased. Delgado *et al.*[12] observed that although the presence of the acidic sites of γ-Al_2O_3 is desirable for dehydration reactions (*i.e.*, for C–O cleavages), it can promote excessive C–C bond cleavage *via* acidic cracking mechanism if there are too many acidic sites.

In order to overcome this drawback, bimetallic catalyst species combined with acidic or basic components were frequently reported for catalyzing glycerol hydrogenolysis.[10] Delgaldo *et al.*[12] reported that the addition of MgO to Cu/Ni/*x*MgO-Al_2O_3 is an alternative to control the acid/base characteristic of the support, achieving a 50% yield of 1,2-PDO without external hydrogen after reacting for 6 h using a fixed-bed reactor. Samudrala *et al.*[13] achieved a high glycerol conversion (86%) and 1,3-propanediol selectivity (42%) by using a continuous vertical fixed bed quartz reactor over the zeolite-based catalyst at 210 °C for 7 h. Priya *et al.*[14] employed the combination of Cu on a mordenite support as a catalyst to improve the selectivity of propanediols, achieving 90% conversion and 58.5% selectivity for 1,3-PDO using vapor phases at 210 °C. The glycerol hydrogenolysis was performed in a fixed-bed flow reactor using NiCu/ZSM-5 and NiCu/γ-Al_2O_3 catalysts at 250 °C under 40 bar of nitrogen gas pressure.[15] The obtained glycerol conversion was 85% and 80% for the NiCu/ZSM-5 and NiCu/γ-Al_2O_3 catalysts, respectively, and both catalysts presented 1,2-PD selectivity at around 25%.

In particular, the manifestation of bimetallic metal oxide catalysts often led to structural instability and metal leaching during large-scale applications, primarily due to suboptimal metal ratios in the impregnated bimetallic oxide catalyst. These imbalances can alter the interaction between the two metals, the overall surface stability, and susceptibility to solvent effects, ultimately impacting the catalytic activity and shortening the catalyst's operational lifespan.[16] Wang *et al.*[16] reported that the association of a Cu metal oxide with a Zn oxide metal in a Cu/Zn : Al ratio of 3 : 1 contributed to the lowest conversion of glycerol at about 34%, with 57% selectivity for propanediols. In contrast, a 6 : 1 Cu/Zn : Al ratio attained the highest conversion, which was about 43% with 69% selectivity. The structures with different ratios of (Cu + Zn)/Al absolutely affected the basicity and acidity strengths with different proportions of the respective salts. Another study proved that the Cu : Zn/Al catalyst with a 2 : 1 ratio was an efficient material for the combined reaction cycle of methanol APR and glycerol hydrogenolysis, obtaining 95.6% glycerol conversion with 79.4% selectivity (76.2% yield) to propanediol.[17] It is believed that metal ratios leading to poor synergistic interactions or structural weaknesses within the catalyst can render active metal sites vulnerable to dissolution and detachment from the solid support, particularly under liquid-phase reaction conditions. More importantly, such ratios may influence the strength of the catalyst's acidity or basicity, further affecting its stability and performance.[18] To mitigate these challenges, synthesis of the bimetallic species with different metal oxide ratios on the support can enhance the structural stability and surface acidity, thereby minimizing metal leaching and improving the overall catalytic performance. It has been well reported in the literature that the mechanism of glycerol hydrogenolysis is strongly influenced by the acid/base character of the reaction medium.[19] In acidic conditions, the hydrogenolysis performs consecutive glycerol dehydration to acetol (on acid sites) and acetol hydrogenation to 1,2-PDO (on metal sites). The glycerol first undergoes dehydrogenation into glyceraldehyde, followed by dehydration into 2-hydroxypropenal (on basic sites), and then hydrogenation into 1,2-PDO.[20,21] Therefore, in this research, bimetallic *x*Cu/*x*Mg was used as an alkaline promoter impregnated on acid Al-MCM-41 support as a catalyst in a batch reactor without external hydrogen gas. The reaction was evaluated using the green solvent ethanol as an *in situ* hydrogen source at 190–220 °C for 1–4 h under N_2 pressure of 5 bar for 1,2-PDO and 20 bar for 1,3-PDO.

Experimental

Materials

The crude glycerol was obtained from Sime Darby Plantation Berhad. Commercial zeolite Al-MCM-41 was purchased from ACS Materials, LLC. Copper(II) nitrate hexahydrate $Cu(NO_3)_2 \cdot 6H_2O$ and magnesium nitrate hexahydrate ($Mg(NO_3)_2 \cdot 6H_2O$) salts were obtained from Merck, Germany.

Method

Catalyst preparation. Commercial zeolite Al-MCM-41 was impregnated with 2.5, 5, 7.5, and 10 wt% copper(II) nitrate hexahydrate salt *via* the incipient wetness impregnation method. A sufficient amount of commercial Al-MCM-41 was fully dissolved in deionized water before Cu nitrate salt was added to the Al-MCM-41 aqueous solution. All catalysts prepared were stirred for 3 h at room temperature, and then dried at 100 °C for 24 h and calcined at 550 °C for 5 h. The same process was repeated to impregnate different ratios of MgO with the synthesized ($x = 2.5$, 5 and 7.5 wt%) *x*Cu/MCM by using $y =$ 2.5, 5 and 7.5 wt% magnesium nitrate hexahydrate salts to synthesize the bimetallic *x*Cu/*y*Mg/MCM.

Catalyst characterization. The crystallization state of the prepared mesoporous materials of Al-MCM-41 supported Cu was determined using X-ray diffraction (XRD) (Bruker model X'Pert3 Powder and Empyrean, PAnalytical) with Cu-Kα radiation. The diffractograms were recorded in the 2θ range of 1–10° (small angle) and 10–80° (wide angle) in 0.010° steps with a 15 s count time at each point.

N_2 absorption–desorption was performed on the Micromeritics ASAP 2020. Textural measurements such as specific surface areas, pore volume, and pore size distribution were obtained according to the Brunauer–Emmett–Teller theory and by the BJH method using N_2 at 78 K. Prior to adsorption, the samples were pretreated under vacuum at 543 K for 3 h.

Catalyst reduction properties were determined by a temperature program reduction using a Thermo Scientific TPDRO 1100 with a TCD detector. The catalysts were treated at 423 K under

the flow of argon (40 mL min^{-1}) prior to reduction. The TPR conditions were as follows: 125 mg of catalyst was reduced at atmospheric pressure under a stream of 5% v/v H_2 in argon (total flow rate of 25 mL min^{-1}), using a linear temperature program from room temperature to 1273 K, with a heating rate of 10 K min^{-1}.

The surface acidity was determined by recording the temperature-programmed desorption (NH_3-TPD) profile of the samples using a Thermo Scientific TPDRO 1100 with a TCD detector. A 100 mg samples were pretreated at 40 °C min^{-1} under He gas with a flow rate of 20 mL min^{-1} for 180 min and then cooled to 50 °C. Subsequently, the samples were exposed to a mixture of 5 vol% NH_3–N_2 for 30 min and then purged by high-purity He gas with a flow rate of 25 mL min^{-1} to remove the physiosorbed NH_3. After the baseline was stable, the sample was heated from 50 °C to 800 °C with the heating rate of 10 °C min^{-1}.

Crude glycerol purification. As the received crude glycerol is solid at room temperature, around 200 g of the crude glycerol was melted at 55 °C in a 500 mL beaker placed on a magnetic hot plate. The molten crude glycerol under gentle stirring was acidified with different acids (sulfuric acid, hydrochloric acid, and phosphoric acid, respectively) to a desired pH level, and was kept for a sufficiently long time to allow the formation of three separate layers. The top layer is the fatty acid phase, the middle one is the glycerol-rich phase and the bottom one is the inorganic salt phase. The bottom phase was separated by simple decantation. The fatty acid-rich top phase was separated from the glycerol-rich phase using a separator funnel. The extracted glycerol was neutralized using 12 M KOH solution, followed by evaporation of water at 110 °C for 2 h and filtration to remove the precipitated salt. The obtained glycerol was further purified by solvent extraction process using methanol as the solvent to promote the precipitation of dissolved salts.[22]

Catalyst testing. The glycerol hydrogenolysis reaction was performed in a 100 mL autoclave stainless steel high-pressure batch reactor equipped with a thermocouple and a motor drive magnetically coupled to an internal stirrer shaft. Prior to the catalytic testing, the catalysts were reduced in a fixed-bed reactor under H_2 flow at 25 mL min^{-1} at 300 °C for 3 h. The reduced catalyst (0.1–0.5 g) and 40 mL of the desired amount of purified dissolved organic solvent were introduced into the autoclave. The reactor was sealed and purged more than three times with pure N_2, and then pressurized up to 5 (for 1,2-PDO) and 20 bar (for 1,3-PDO). The tested reaction conditions were as follows: 180–220 °C, 40 mL purified glycerol dilute in different organic solvents (water, ethanol, and methanol), 0.1 to 0.5 g of catalyst, and 250 rpm stirring rate. After each reaction time, the system was cooled to room temperature, and the catalyst was separated by centrifugation at 2000 rpm for 10 min or filtered using a vacuum pump.

Product characterization. The separation of the compounds was performed on a Polaris Hi-Plex H column, 300 × 7.7 mm, using the 5 mM H_2SO_4 mobile phase with a flow rate of 0.6 mL min^{-1}, column temperature $T = 80$ °C, and RID temperature $T = 35$ °C. The elution of the compounds was run for 25 minutes. The yield of 1,2/1,3-PDO and glycerol conversion were measured quantitatively using the calibration curve at five different concentrations (SI). To prepare a calibration curve of the product, each working standard solution with diverse concentrations was injected into the HPLC system. Afterward, the curve was plotted based on measuring the peak area obtained from the injected aliquot of standard 1,2/1,3-PDO and glycerol solution with known concentration. This was employed to quantitatively determine the 1,2/1,3-PDO yield and glycerol conversion.

Results and discussions

Catalyst characterization

The XRD patterns for all catalysts are shown in Fig. 1. Fig. 1(a) displays the low-angle diffraction peaks (1–10°) of Al-MCM-41 with different loadings of monometallic Cu/MCM and

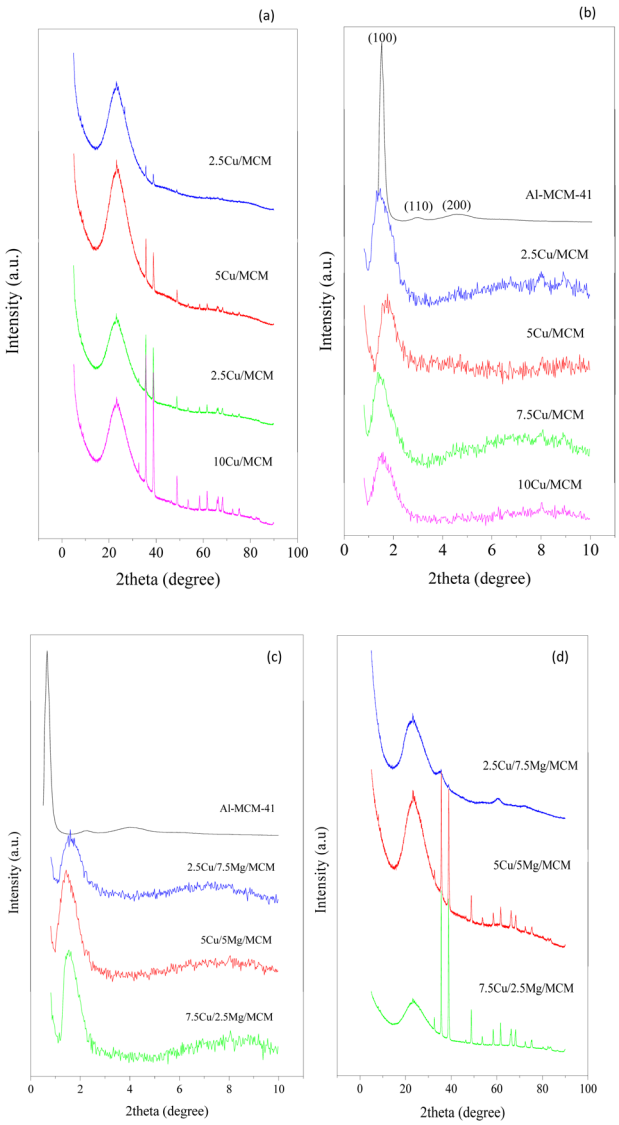

Fig. 1 X-ray diffraction analysis of (a) low-angle monometallic Cu/MCM, (b) wide-angle monometallic Cu/MCM, (c) low-angle bimetallic Cu/Mg/MCM and (d) wide-angle bimetallic Cu/Mg/MCM.

bimetallic Cu/Mg/MCM. A strong peak is assigned to the (100) plane, formed at $2\theta = 2.1°$. Meanwhile, two other diffraction peaks with low intensity, centered at approximately $2\theta = 3.8°$ and 4.4°, correspond to the (110) and (200) planes, respectively, according to ICSD 98-015-4906. The formation of the (100), (110), and (200) planes is attributed to the highly ordered two-dimensional hexagonal arrangement of the MCM support.[23] In Fig. 1a and c, the characteristic peaks on plane (100) can be observed, indicating that the framework of MCM-41 remains unchanged upon impregnation of Cu and Mg on the mesoporous MCM-41 matrix. It should be noted that the peak intensities of the modified samples gradually decrease with the increase in metal incorporation, suggesting that a less ordered structure was formed. Additionally, the intensity of the MCM-41 peak consistently decreases as the Cu loading increases from 2.5 to 10 wt% in monometallic samples.

Meanwhile, different Cu/Mg bimetallic ratios show no significant intensity change for 1 : 1 and 3 : 1 Cu/Mg ratios. However, the deposition of the Cu and Mg metal pairs at a 1 : 3 ratio results in a lower-intensity diffraction peak at the (100) plane, suggesting that Mg dominates the deposition on the support as its ratio increases relative to Cu. The shift in the (100) diffraction peak of all bimetallic Cu/Mg samples toward higher 2θ values (Fig. 1(c)) is possibly related to the incorporation of Cu and Mg metal species into the pores, leading to a reduction in pore size and compressive lattice strain.[24] The wide-angle (20–80°) X-ray diffraction patterns of the Al-MCM-41 and Cu/Mg/MCM catalysts with different loadings and ratios are presented in Fig. 1b and d. The XRD spectra of Cu exhibit two peaks at $2\theta = 35.5°$ and 38.7°, attributed to the CuO phase (ICSD 98-008-7122), which correspond to the Miller indices (002) and (111), respectively. In contrast, two diffraction peaks at $2\theta = 61.6°$ and 74.5° indicate the formation of the Mg species and are assigned to the (220) and (311) planes, respectively, as referenced in ICSD 00-04500946. The spectral signal for CuO formation increases as the ratio of Cu increases. Meanwhile, the spectra signal of MgO was detected at low intensity at higher Mg ratio as compared to Cu metal.

Nitrogen monolayer adsorption on the mesopore walls accounts for adsorption on Al-MCM-41 materials at low relative pressures ($P/P_0 < 0.3$) for different loading amounts of monometallic Cu/MCM-41, as depicted in Fig. 2. The relative pressure position of the inflection point is correlated with the mesopore diameter. Moreover, the isotherms show sharp inflections typical of capillary condensation within uniform mesopores. Meanwhile, in bimetallic cases, a relative pressure higher than 0.4 is characteristic of a typical three-stage isotherm of mesopore monolayer adsorption on the mesoporous walls, capillary condensation within the mesopores, and multilayer adsorption on the mesoporous surface, corresponding to type IV isotherms.[25] According to the IUPAC references, all calcined samples of mono- and bi-metallic species impregnated on supports exhibited type IV adsorption–desorption isotherms, displaying the shape typical of Al-MCM-41-based uniform mesoporous materials.[26]

The surface area, pore size, pore volume, and crystallite size are summarized in Table 1. The surface area between Al-MCM-41 and 2.5Cu/MCM decreases when 2.5 wt% of Cu is impregnated into the MCM-41 catalyst. This indicated an interaction of the Cu species with the surface and pores of MCM. A study done by Rahman *et al.*[27] reported that a different decreasing pattern between MCM-41 and Ni/MCM-41 can be observed from the textural properties, which indicates the blocking of pores by the deposition of NiO into the MCM-41 support. The surface area was observed together with the pore volume, which also demonstrated a decrease in value. However, as the loading of the impregnated Cu increases from 7.5 to 10 wt%, it can be observed that the surface area and pore volume decrease

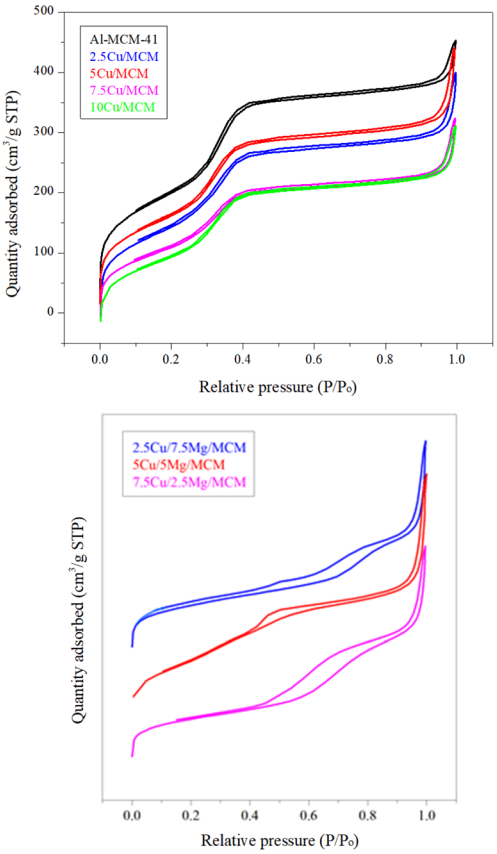

Fig. 2 Isotherm linear plots of Al-MCM-41, monometallic Cu/MCM and bimetallic Cu/Mg/MCM.

Table 1 Textural properties of Al-MCM-41 with different loadings of monometallic Cu/MCM and different ratios of bimetallic Cu/Mg/MCM

Catalyst	Surface area ($m^2\ g^{-1}$)	Pore size (nm)	Pore volume ($cm^3\ g^{-1}$)	Crystallite size (nm)
Al-MCM-41	745	3.48	0.78	9.7
2.5Cu/MCM	617	3.80	0.69	15.1
5Cu/MCM	692	3.89	0.82	14.2
7.5Cu/MCM	501	3.95	0.54	16.4
10Cu/MCM	492	3.68	0.56	12.7
2.5Cu/7.5Mg/MCM	237	3.49	0.37	12.9
5Cu/5Mg/MCM	295	3.47	0.31	10.8
7.5Cu/2.5Mg/MCM	309	4.23	0.34	13.3

significantly except for the 5Cu/MCM catalyst. The decreased nitrogen uptake indicated a limitation of the mesopore volume in these samples due to the incorporation of copper into MCM-41.[28] For 5Cu/MCM cases, there is a contradiction in both surface area and pore volume compared to other catalysts. The contradict textural properties observed for their 5Cu/MCM catalyst are primary attributed to the preferential deposition Cu particles on the external surface of the support, rather than within its mesoporous channels.[29]

After incorporation of both Cu and Mg, the surface area of the bimetallic catalyst was found to be lower than the monometallic catalyst with Cu. As for the bimetallic Cu/Mg/MCM species, the observed textural properties were significantly distinct with different Cu/Mg ratios on the support. The surface area was significantly reduced when the amount of Cu incorporated was higher relative to Mg. A similar trend was observed for the pore volume and pore size, where the amount of Cu was greater than or equal to the Mg loading on the support (Table 2). There are slight differences that can be observed in the pore size for all catalysts. In comparison with the support, all the catalysts show a decrease in surface area and pore volume. Thus, incorporation of the active metals changes the uniform mesoporous characteristic of the catalysts (Table 1).[25]

The size of the Al-MCM-41 particles was calculated from the XRD line broadening of the peak at the (100) plane, using Scherrer's equation for all catalysts. The zeolite support particle size for all catalysts shows a decreasing pattern as the Cu content increases. This observation may be due to the uniform distribution of the metal particles in the large surface area of the MCM-41 support, as described by Mallesham *et al.*[30] As for the bimetallic Cu/Mg/MCM species, the particle size decreases when the Cu content increased to 5 wt%. As it reached 7.5 wt% Cu, the particle size was observed to decrease. The changing pattern in the XRD spectra of Cu/Mg/MCM is due to the interference of copper and magnesium ions during the formation of ordered structures. This leads to increased order and pore blocking, which could also be responsible for the uneven trend of sample textural properties, as shown in Table 1.

Fig. 2 displays the H_2-TPR profiles of the monometallic species of different Cu loading and bimetallic species of different Cu/Mg ratios on the Al-MCM-41 support. Al-MCM exhibits low-intensity peaks that appear in the temperature range of 56 °C to 791 °C with a total of four continuous broad peaks centered at 56 °C, 353 °C, 584 °C, and 791 °C, while there are three broad shoulders formed at around 272 °C, 654 °C, and 696 °C. Additionally, the intensity of the peak of Al-MCM-41 shows a noticeable difference compared to that of MCM supported by different loadings of Cu. All Cu/MCM catalysts with different loading display a sharp and prominent reduction peak at substantially low-temperature regions. As Cu was introduced into the support, we observe that the MCM reduction peak slowly vanished as it shifted to lower and higher temperature regions with increasing Cu content. The reductions of sharp peaks centered at 277 °C and 305 °C are associated with the reductions of Cu^{2+} to Cu^0 in the aggregated copper oxide species and $Cu^{2+} \rightarrow Cu^+$ in the monomeric copper cations, respectively, while the second peak is assigned to the second step of the monomeric cation reduction of $Cu^+ \rightarrow Cu^0$.[31] In 2.5Cu/MCM and 5Cu/MCM, the Cu ions are dispersed with a lower reduction of the Al_2O_3 species as it shifted to a lower temperature, and gave rise to the reduction peak at around 270 °C to 310 °C.[32] On the other hand, a broad peak detected around 870 °C for the 7.5Cu/MCM and 10Cu/MCM catalysts indicated that the SiO_2 species shifted to a higher temperature region of more than 800 °C as the Cu loading increased. The reduction of copper silicate was not complete below 800 °C, as the copper species was occluded in the silica walls of MCM-41 and copper silicate is also resistant to reduction.[33]

Meanwhile, the observation of multiple broad and shoulder peaks at temperatures above 450 °C indicates the incorporation of the Mg species on the MCM support for all bimetallic Cu/Mg species. The reduction peaks of the MgO–Al_2O_3 species were fully overlapped, resulting in a broad shoulder formation centered at around 463 °C.[34] This observation was most evident for the Cu/Mg catalyst with a 1 : 3 ratio where peak profiles showed the dominate broad peak of higher content of Mg than Cu. Thus, the H_2 intake showed a decreasing pattern with higher MgO content on the MCM support.[10] One sharp peak and three broad peaks were also detected at 348 °C, 644 °C, 841 °C and 933 °C, respectively. As mentioned in a previous discussion, the appearance of a reduction peak at 348 °C corresponds to the complete reduction series of the Cu species to metallic copper without the formation of the intermediate copper oxide species, which is in agreement with the previous literature.[35]

Table 2 Reduction properties of the synthesized monometallic Cu/MCM and bimetallic Cu/Mg/MCM[a]

	Hydrogen uptake (μmol H_2/g)					
Catalyst	Peak 1	Peak 2	Peak 3	Peak 4	Peak 5	Total
*	2707.9	2869.6	2845.0	2878.9	n.d.	11 301.4
2.5Cu*	3978.7	3085.1	453.1	873.2	n.d.	8390.1
5Cu*	12 813.4	1070.6	565.7	n.d.	n.d.	14 449.7
7.5Cu*	21 516.0	20 319.2	861.8	n.d.	n.d.	42 697.0
10Cu*	32 749.1	30 500.5	854.5	n.d.	n.d.	64 104.1
2.5Cu/7.5Mg*	11 360.3	12 954.4	12 524.9	9669.5	9832.2	56 341.3
5Cu/5Mg*	51 788.9	3056.6	4627.7	n.d.	694.0	60 167.2
7.5Cu/2.5Mg*	619 441.1	13 917.2	10 233.2	n.d.	10 441.9	654 033.4

[a] (*) = Al-MCM-41 support, n.d. = not detected.

All catalysts presented the maximum reduction peak at the temperature range of 330 °C to 350 °C, which is higher than those of the $MgO–Al_2O_3$ catalysts, suggesting that CuO and MgO crystals may have stronger interactions with the Al-MCM-41 support lattice.[36] In the meantime, the other reduction peak centered at 644 °C corresponds to the reduction of the lattice of Mg^{2+} in the $MgO–Al_2O_3$ solid solution. This band is more intense for the 1 : 3-ratio Cu/Mg bimetallic species on the MCM catalyst. The presence of two small reduction bands at 841 °C and 933 °C can be assigned to the partial MgO present in the $MgO–Al_2O_3$ solid-solution since it cannot be fully reduced. They are rather difficult to reduce by hydrogen due to the high reducibility temperature of the Al-MCM-41 support.[32] As observe in Fig. 3, the intensity of the MgO reduction peak showed gradually decreased as the MgO content were reduced from 7.5 wt% to 2.5 wt%. For the Cu/Mg bimetallic catalyst with a 1 : 1 ratio, one high sharp and three broader peaks with low reduction uptake detected occur at 332, 411, 475 and 835 °C, respectively. On the other hand, the same pattern was observed for the 3 : 1-ratio Cu/Mg bimetallic species on a MCM support with reduction peaks centered at 326 °C, 398 °C, 587 °C and 904 °C. The CuO metal showed a dominant sharp peak as the Cu content increased from 2.5 wt% to 7.5 wt%.

Table 2 summarizes the hydrogen uptake of Al-MCM-41, monometallic Cu/MCM and bimetallic Cu/Mg species on the MCM catalyst. The total hydrogen consumption of the Cu/MCM catalyst decreases at 2.5 wt% of Cu content, and gradually increases as the Cu content increases to 5, 7.5, and 10 wt%. The increase of the hydrogen uptake with higher Cu content is probably due to the contribution of Al_2O_3 and SiO_2 in MCM to promote the reduction of the easily accessible surface copper species at lower temperature regions.[31] Meanwhile, for the bimetallic Cu/Mg cases, an increasing trend was observed for the total hydrogen uptake as the Cu content was larger than Mg on the support. The synergistic interaction between Cu and Mg in the support shifted the reduction temperature to lower values when MgO was introduced. This effect confirms the occurrence of hydrogen spillover from MgO when Cu content exceeded that of Mg.[37] Generally, the migration of activated hydrogen species (H atoms, H^+/e^- pairs) proceeds from a metal catalyst to a support material. In Cu–MgO systems, Cu dissociates H_2 into atomic hydrogen, which then migrates onto MgO as its non-reducible oxide. The ability of the MgO metal to accept and transport hydrogen depends heavily on the presence of sufficient metal sites.[38,39]

The order of reducibility for the catalysts demonstrated that 7.5Cu/2.5Mg/MCM exhibited the highest hydrogen uptake, followed by 5Cu/5Mg/MCM and 2.5Cu/7.5Mg/MCM.

Fig. 4 displays the NH_3-TPD analysis of Al-MCM-41, along with different contents of Cu monometallic and bimetallic catalysts with different ratios of Cu/Mg on the MCM support. As illustrated in Fig. 4, the NH_3-TPD profiles of all synthesized catalyst revealed three distinct distributions of acid strength, corresponding to weak, moderate and strong acid sites. For Al-MCM-41, the acid site can be classified as weak at the temperature region of 50–200 °C, followed by moderate acid sites at the temperature range of 150–350 °C, and strong acid sites at temperatures above 350 °C.[38] The ammonia desorption profile is spread in a relatively broad temperature range and consists of three unresolved maxima, indicating significant heterogeneity of the acid site strength. The result reveals that there are three distinguished broad peaks detected for the Al-MCM-41 catalyst located at moderate and strong region sites, which indicate its highly acidic properties as previously reported.[31] The acid strength of Al-MCM-41 is mostly contributed by the incorporation of the aluminum species into MCM-41 as desorption peaks appeared with high intensity on the moderate and strong acid sites, as depicted in Fig. 4, which agreed with the literature.[40] According to,[41] desorption peak formed in range of 150–170 °C corresponds to week acid sites associated with surface hydroxyl group. Peak appearing at range 170 to 350 °C are attributed to

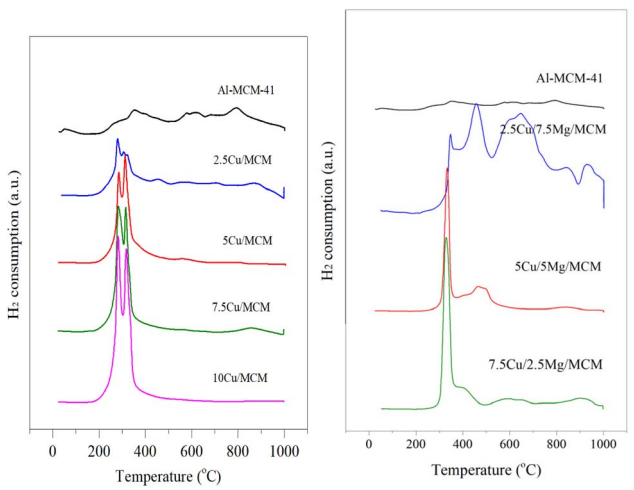

Fig. 3 H_2-TPR analysis of Al-MCM-41, monometallic Cu/MCM and bimetallic Cu/Mg/MCM.

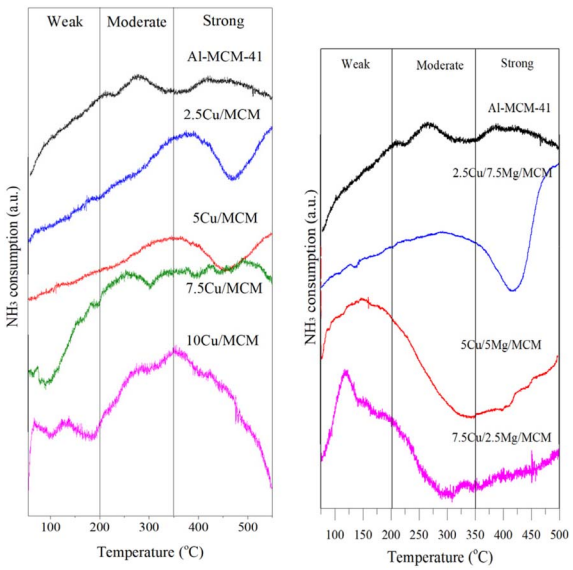

Fig. 4 NH_3-TPR analysis of Al-MCM-41, monometallic Cu/MCM and bimetallic Cu/Mg/MCM.

moderate acid sites owing to the presence of trivalent aluminium located in two different framework positions, which contribute to strong Brønsted acidity. The presence of a peak at 350–450 °C is attributed to the weak Lewis acid sites that was caused by the tricoordinated aluminium species. Meanwhile, the desorption peak at a temperature above 450 °C corresponds to the dislodgement of aluminium from the framework structure, leading to the formation of aluminium oxide clusters (strong Lewis group).[42]

As observed in Fig. 3, there are two broad peaks were detected for 2.5Cu/MCM and 5Cu/MCM with desorption peaks shifted at a strong acid region from moderate site as compared to Al-MCM-41 when low Cu content induced into MCM support around more than 350 °C. Copper ions can introduce Lewis acid sites, particularly through the Cu^{2+} species, which interact with ammonia molecules. These sites typically result in medium-to-strong acid strength sites, as previously reported.[31] Additionally, upon increasing the Cu content as the impregnated metal, the desorption peaks of strong acid sites shift to slightly moderate acid sites for 7.5Cu/MCM and 10Cu/MCM. The deposited Cu metal on the support surface acts as Lewis acid sites and are bound to ammonia by donation of a free electron pair into the unoccupied d-orbitals of Cu ($NH_3 \rightarrow Cu$). Hence, the number of such copper sites depend on Cu loading and its surface accessibility.[43] The result is in line with the H_2-TPR (Fig. 3) studies, which show a significant contribution of aggregated copper oxide species as the Cu content increased for both 7.5Cu/MCM and 10Cu/MCM catalysts.

The addition of the Mg species also seems to change the acidity strength of the sample. As observed in Fig. 4, all catalysts show a shift to lower desorption temperature as the Mg content increased from 2.5 wt% to 7.5 wt% in the bimetallic Cu/Mg/MCM samples. According to García *et al.*,[44] the peaks of the samples shifted and slightly decreased in acid strength when MgO was introduced. Their results indicate that the addition of Mg^{2+} species induced the new acid strength by shifted the desorption peak from moderate acid to weak acid regions and most likely the Mg–O sites associated with the MCM support. A research study by Vinu *et al.*[45] reported that the lower acidity of MgO was attributed to the formation of a MgO cluster inside the mesopores of the Al-MCM-41 support channel during the calcination process due to the weak nature of the Mg–O–Si bonds and might block acid sites. In general, the result demonstrated that interaction between Cu/Mg resulting in less acidic strength of Al-MCM-41.

Table 3 summarizes the acid site densities of all synthesized catalysts. The acid site densities of the monometallic Cu/MCM catalyst gradually decreased as the Cu content increased from 2.5 wt% to 10 wt%. The decreasing trend in acid sites as higher content of Cu is suggested due to the strong interaction between support and CuO particles. The introduction of copper into the zeolitic samples significantly modified their surface acidic properties, which resulted in shifting the desorption peaks to lower temperatures.[46] The same trend was observed for bimetallic Cu/Mg/MCM, where the acid site density shows a decreased profile as the Cu content became greater than Mg, as tabulated in Table 3. The lower acid site density observed at reduced Mg content can be attributed to the smaller number of divalent Mg^{2+} ions incorporated into the lattice. This result in fewer negative charges, which are balanced by a corresponding lower number of protons, thereby diminishing the overall acidity.[45]

Table 3 Acid site density of the Cu/MC and Cu/Mg/MCM catalysts[a]

Catalyst	Acid sites (μmol g^{-1})				Acid site density (μmol m^{-2})
	Weak	Moderate	Strong	Total	
*	n.d.	8721.9	7221.1	15 943.0	21.4
2.5Cu*	n.d.	—	10 831.7	10 831.7	17.5
5Cu*	n.d.	5921.3	4788.8	10 710.1	15.5
7.5Cu*	212.9	4897.0	4474.4	10 608.6	21.2
10Cu*	455.3	5977.0	n.d.	6432.3	13.1
2.5Cu/7.5Mg*	n.d.	489.4	3481.0	3970.4	16.8
5Cu/5Mg*	2855.2	n.d.	392.2	3247.4	11.0
7.5Cu/2.5Mg*	1231.4	n.d.	104.7	1336.1	4.3

[a] (*) = Al-MCM-41 support, n.d. = not detected.

Catalyst screening. The catalytic performance of the synthesized catalysts was evaluated using a high-pressure batch reactor, in terms of glycerol conversion and yield towards the production of propanediols. Using the catalytic screening approach, only selected catalysts that give the highest yield of propanediols proceeded for further optimization. Glycerol hydrogenolysis was carried out using ethanol as solvent and 0.2 g of catalyst with 10 wt% of glycerol feedstocks under 5 and 15 bar of inert N_2 for 1,2-PDO and 1,3-PDO, respectively, at 180 °C for 2 h. During the experimental screening, identical reaction parameters were applied for the synthesis of both 1,2-propanediol (1,2-PDO) and 1,3-propanediol (1,3-PDO), with the exception of pressure, which was varied due to the differing requirements of each pathway. The hydrogenolysis of glycerol to produce 1,2-PDO, catalyzed by copper-based systems, typically operates optimally under moderate pressure conditions.[14] However, elevated pressure may lead to undesirable side reactions, including over-hydrogenation and reduced selectivity, resulting in the formation of byproducts such as methanol, acetol, and ethylene glycol. These arise primarily from C–C bond cleavage within the glycerol backbone.[21]

In contrast, the selective hydrogenolysis of glycerol to yield 1,3-PDO necessitates higher pressure to facilitate the hydrogenation of the 3-hydroxypropanal intermediates, which are thermodynamically less stable than those leading to 1,2-PDO. Consequently, the nitrogen pressure settings were adjusted accordingly, with 5 bar applied for the 1,2-PDO synthesis and 15 bar for 1,3-PDO.[47]

From the screening result in Table 4, the 7.5Cu/MCM and 10Cu/MCM catalysts give the highest yields of 1,2-propanediol and 1,3-propanediol compared to other catalysts. In contrast, 2.5Cu/MCM and 5Cu/MCM only selectively produced 1,2-propanediol. Meanwhile, in the case of bare MCM-41, no propanediols were attained. The highest conversion of glycerol to 1,2-propanediols and 1,3-propanediols was 30.8% and 23.1% with selectivity of 18.25% and 14.6%, respectively, when

Table 4 Catalyst screening of the synthesized catalyst for the production of propanediol[a]

	1,2-Propanediol		1,3-Propanediol	
Catalyst	Conversion of glycerol (%)	Yield (%)	Conversion of glycerol (%)	Yield (%)
MCM-41	n.d.	n.d.	n.d.	n.d.
2.5Cu/MCM	24.1	2.0	n.d.	n.d.
5Cu/MCM	23.9	2.1	n.d.	n.d.
7.5Cu/MCM	30.5	5.4	20.4	2.0
10Cu/MCM	**30.8**	**5.6**	**23.1**	**3.4**
2.5Mg/MCM	17.5	1.9	n.d.	n.d.
5Mg/MCM	17.1	1.7	n.d.	n.d.
7.5Mg/MCM	18.0	1.8	n.d.	n.d.
10Mg/MCM	17.9	1.7	3.5	0.01

[a] n.d. = not detected.

employing 10Cu/MCM as a catalyst. Whereas, utilizing the 7.5Cu/MCM catalyst resulted in a conversion of 30.5% (1,2-PDO) and 20.4% (1,3-PDO), and a selectivity of 17.7% (1,2-PDO) and 9.8% (1,3-PDO).

The combination of Cu as an alkaline metal into acid catalysts has been proven to enhance the catalytic performance for propanediol production.[48] The Cu-based catalyst exhibits excellent selectivity towards propanediols due to its properties, which are attributed to the tendency towards selective cleavage of the C–O bond rather than the C–C bond. It has been described that the alkaline metal (or specifically Cu) can promote the cleavage in the C–O bond of the primary hydroxyl group of glycerol to form acetol with a simultaneous H_2 donor from an organic liquid through hydrogenolysis without cleaving the C–C bond of glycerol molecules.[49] Meanwhile, formation of 1,3-PDO is accomplished by the secondary hydroxyl from glycerol being dehydrated into 3-hydroxypropionaldehyde (3-HPA) on Brønsted acid sites, which is then hydrogenated on copper (Cu) metallic sites into 1,3-PDO.[8] The TPR result showed that both 7.5Cu/MCM and 10Cu/MCM catalysts were recorded with high H_2 uptake and were easily reducible at low temperatures. Thus, 7.5Cu.MCM and 10Cu/MCM catalyst fit for the conversion of glycerol to propanediols by improving the selectivity to cleavage the C–O bond where it can be proved by the highest conversion and selectivity towards both 1,2-propanediols and 1,3-propanediols production as shown in Table 4. A benchmark comparison from previous studies is summarized in Table 5 to compare the catalytic performance of the synthesized bimetallic Cu/Mg/MCM catalyst with other catalysts for the production of propanediols.

The studies on glycerol hydrogenolysis highlight several promising catalytic systems with varying efficiencies and selectivities. Ni–Cu/AlO(OH) catalysts showed strong performance. Meanwhile, incorporating MgO into Cu/Ni/*x*MgO-Al_2O_3 provided a route to control the acid–base properties of the support. The NiCu/ZSM-5 and NiCu/γ-Al_2O_3 catalysts delivered high glycerol conversions, although their selectivity to 1,2-propanediol was relatively low. In contrast, Pt-*x*Re/WO_3/ZrO_2 catalysts demonstrated exceptional results under mild hydrogen pressure, with 96.8% conversion and 95.2% selectivity to 1,2-propanediol. The synthesized Ir–ReO_x/SiO_2 catalysts directed the reaction toward 1,3-propanediol, suggesting that catalyst design can steer product distribution toward different diols.

Catalyst testing

Effect of the solvent system as *in situ* H_2. Fig. 5 shows the effect of the different solvent systems (ethanol, methanol, and water) on propanediol production at 180 °C for 2 h and catalyzed by 10Cu/MCM under 5 and 20 bar of inert N_2 for the production of 1,2-PDO and 1,3-PDO. It was found that the use of ethanol as a solvent resulted in the highest conversion and selectivity of propanediols for both 1,2-PDO and 1,3-PDO, followed by methanol and water. The *in situ* hydrogen production

Table 5 Benchmarking catalysts for the production of propanediols

Catalyst	Findings	Ref.
Ni–Cu/AlO(OH)	Optimization of Ni and Cu loading on the support achieved the highest catalytic performance with 25 wt% Ni and 15 wt% Cu at 240 °C and 550 psi hydrogen pressure using 4 wt% catalyst loading, resulting in 92.7% 1,2-PD selectivity and 60.3% yield with 65.1% glycerol conversion in 6 h	50
Cu/Ni/*x*MgO-Al_2O_3	Addition of MgO to Cu/Ni/*x*MgO-Al_2O_3 is an alternative to control the acid/base characteristic of the support that gives 50% yield of 1,2-PDO without external hydrogen after 6 h reaction using a fixed-bed reactor	12
NiCu/ZSM-5 and NiCu/γ-Al_2O_3	The glycerol hydrogenolysis performed in a fixed-bed flow reactor using NiCu/ZSM-5 and NiCu/γ-Al_2O_3 catalysts at 250 °C under 40 bar of nitrogen gas pressure that achieved glycerol conversion of 85% and 80% for the NiCu/ZSM-5 and NiCu/γ-Al_2O_3 catalysts, respectively, and both the catalysts presented 1,2-PD selectivity at ~25%	15
2Pt-*x*Re/WO_3/ZrO_2	The hydrogenolysis of glycerol was carried out in a fixed bed reactor in the presence of 2Pt-*x*Re/WO_3/ZrO_2 catalyst under atmospheric H_2 pressure (0.1 MPa), affording 96.8% glycerol conversion and a good selectivity of 1,2-propanediol at 95.2%	51
Ir–ReO_x/SiO_2	The hydrogenolysis of glycerol to 1,3-propanediol over the Ir–ReO_x/SiO_2 catalyst was performed in a 190 mL stainless steel autoclave with an inserted glass vessel at 160 °C under 3 MPa of pressure for 4 h, successfully converting 78% of glycerol with 69% selectivity to 1,3-propandiol	52

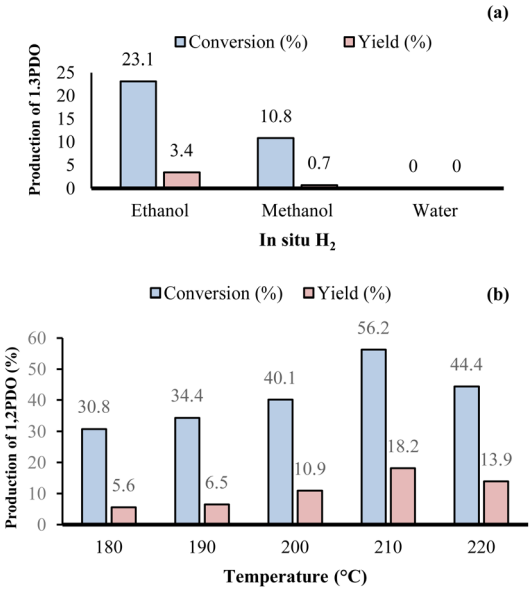

Fig. 5 Effect of the solvent system as *in situ* H_2, reaction conditions: (a) 180 °C, 4 h, 0.2 g of 10Cu/MCM, 10 wt% of glycerol feedstocks, 20 bar of N_2 (1,3-PDO); (b) 180 °C, 4 h, 0.2 g of 10Cu/MCM, 10 wt% of glycerol feedstocks, 5 bar of N_2 (1,2-PDO).

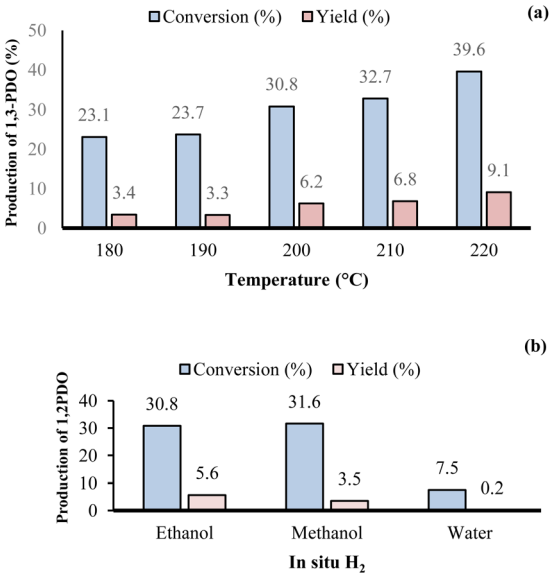

Fig. 6 Effect of the reaction temperature, reaction conditions: (a) 4 h, 0.2 g of 10Cu/MCM, 10 wt% of glycerol feedstocks in ethanol, 20 bar of N_2 (1,3-PDO); (b) 4 h, 0.2 g of 10Cu/MCM, 10 wt% of glycerol feedstocks in ethanol, 5 bar of N_2 (1,2-PDO).

aided by ethanol was consumed during the hydrogenation of the intermediate acetol to propanediols over Cu metal. The hydrogen dehydrogenated from ethanol exists mainly in the form of the active hydrogen atom, which is adsorbed on the surface of the catalyst and enhanced to react with acetol quickly, which is the reason for the high conversion and selectivity of propanediols.[53] Furthermore, the high efficiency of ethanol as an *in situ* hydrogen source could be attributed to the active sites provided by Cu for the dehydrogenation of ethanol. This finding is in agreement with the works by Chang *et al.*[53] and Carotenuto *et al.*,[54] which stated that ethanol (as a competent *in situ* hydrogen source) together with the Cu metal improved the active site and selectivity for accelerating the acetol intermediate formation for the further hydrogenation to form propanediol.

Effect of the reaction temperature. Fig. 6 demonstrates the reaction temperatures on glycerol hydrogenolysis over 10Cu/MCM using ethanol as *in situ* hydrogen for 2 h with 10 wt% of glycerol feedstocks at various temperatures from 180 to 220 °C. As expected, the conversion of glycerol to 1,3-PDO °C showed a notable increase when the reaction temperature was raised from 180 °C to 220 °C. Meanwhile, the yield of 1,3-PDO also improved as the temperature increased from 180 °C to 220 °C. This was due to the improvement of the reaction temperature, which favored glycerol conversion and led to high propanediol production. According to Mauriello *et al.*[55] and Ramesh *et al.*,[56] the increased reaction temperature could be related to the improved hydrogen production activity, as well as the decrease of the reaction mixture viscosity at high temperature. A low glycerol conversion was noticed due to insufficient temperature at 180 °C to activate the reactant molecules and surface-active sites.[56] The conversion and yield to 1,2-propanediol were found to improve as the temperature increased. However, as the temperature increased to 220 °C, there was a sharp decline in the conversion and yield for 1,2-PDO production, accompanied with the higher production of ethylene glycol and ethanol as lower three-carbon by-products. In contrast, the production of lower three-carbon by-products did not significantly change at temperatures higher than 210 °C for 1,3-PDO production. From these results, it is suggested that the reaction temperature of 220 °C is more favorable for the dehydration of the secondary hydroxyl group of glycerol, making the hydrogenolysis reaction more selective to 1,3-PDO. Meanwhile, dehydration of the primary hydroxyl group of glycerol likely occurs at 210 °C for 1,2-PDO cases.[13]

Effect of reaction duration. The effect of the reaction duration on the conversion of glycerol and yield of 1,2-PDO and 1,3-PDO was investigated, and the results are depicted in Fig. 7. As the reaction progressed, both the glycerol conversion and the yield of 1,3-PDO gradually increased. At 4 h, the highest glycerol conversion of 33% and 1,3-PDO yield of 7.2% were acquired. The same goes with the conversion and yield of 1,2-PDO, where it showed an improvement upon extending the reaction duration from 1 to 3 h. However, the maximum conversion and yield subsequently dropped when the reaction time was extended to 4 h. The glycerol conversion of 1,2-PDO significantly dipped from 56.6% to 49.8%, whereas a considerable decrease in the yield of 1,2-PDO was observed from 17.7% to 15.4% at the end of the 4 h reaction duration. It could be concluded that a reaction time of 3 h was sufficient to produce enough active sites for glycerol conversion and 1,2-PDO formation. However, when the time was extended to 4 h, it might have led to the aggregation of active Cu species, thus allowing for coke formation. This could lower the probability of C–O hydrogenolysis and increase the

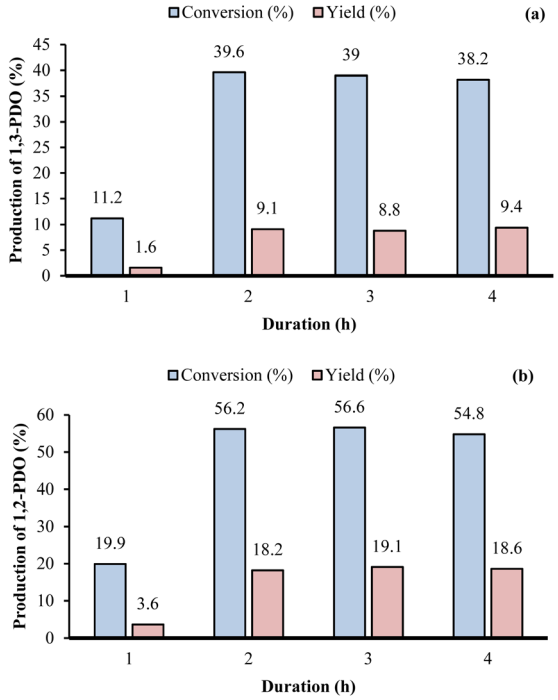

Fig. 7 Effect of reaction duration, reaction conditions: (a) 220 °C, 0.2 g of 10Cu/MCM, 10 wt% of glycerol feedstocks in ethanol, 20 bar of N_2 (1,3-PDO); (b) 210 °C, 0.2 g of 10Cu/MCM, 10 wt% of glycerol feedstocks in ethanol, 5 bar of N_2 (1,2-PDO).

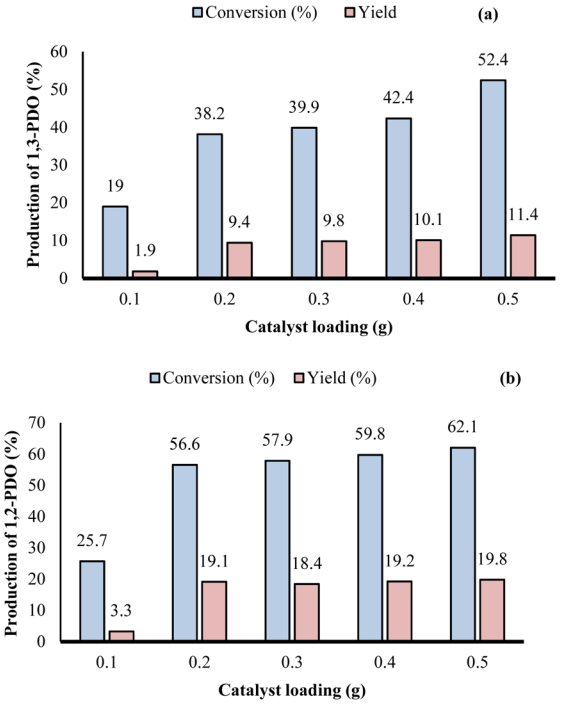

Fig. 8 Effect of catalyst loading, reaction conditions: (a) 220 °C, 4 h, 10 wt% of glycerol feedstocks in ethanol, 20 bar of N_2 (1,3-PDO); (b) 210 °C, 3 h, 10 wt% of glycerol feedstocks in ethanol, 5 bar of N_2 (1,2-PDO).

formation of degradation products in higher amounts, which may also be due to the faster deactivation of acid sites in the catalyst system.[13]

Effect of catalyst loading. Fig. 8 shows the effect of catalyst loading on the catalytic performance of the 10Cu/MCM catalyst by varying the loading from 0.1 g to 0.5 g. At the lowest catalyst loading, the glycerol conversion and 1,2-propanediol yield were found to be 25.7% and 3.3%, respectively. As the loading of the catalyst increasing to 0.5 g, the glycerol conversion increased to 62.1% and 19.8%, respectively. The conversion of glycerol and yield of 1,3-PDO also showed the same increasing pattern with 19% and 9.1%, respectively, at low catalyst loading. A high conversion of glycerol and production of 1,3-PDO was achieved at the highest catalyst loading. This result indicates that the active sites provided on the surface of the Cu/MCM catalyst sufficiently accelerate the conversion of glycerol to propanediols. Moreover, as the catalyst loading increased, glycerol suppressed toward the cleavage of C–C bond, favoring sequential of hydrogenolysis pathway on the available active sites that enhance selectivity towards propanediol formation. However, it also led to condensation reactions between the acetol intermediate and other alcohols, which resulted in a higher yield of ethylene glycol and other lower three-carbon by-products at higher catalyst loading.[13] Priya *et al.*[14] suggest that as the catalyst loading increases, the number of active sites to react with glycerol also increases, becoming most likely sufficient to convert excess glycerol. Thus, the other product distribution also showed the selectivity towards the formation of ethylene glycol and ethanol with a uniform increase with the increased catalyst loading.

Effect of using monometallic and bimetallic catalyst species. The synthesized catalysts in this study exhibited comparable catalytic activity in terms of glycerol conversion and propanediol production (Fig. 9). The glycerol conversion was lower for the monometallic Cu/MCM catalysts than for the bimetallic Cu/Mg/MCM catalysts. Interestingly, the 7.5Cu/2.5Mg/MCM catalyst showed a high glycerol conversion of 79.5% and 27.4% yield of 1,2-propanediol. Meanwhile, for the 1,3-propanediol cases, the glycerol conversion was 78.2% with 11.5% yield. The observed high conversion and yield values for the propanediols using the bimetallic 7.5Cu/2.5Mg/MCM (3 : 1) catalysts were due to the acidic and basic nature of the active surface sites and the fact that the synergistic nature played an essential role in the catalytic activity. In a bifunctional process, the hydrogenolysis reaction involves two crucial steps to transform glycerol into PDO: the dehydration of glycerol to 3-hydroxy propionaldehyde (3-HPA) over acidic sites (zeolite species), followed by hydrogenation of the intermediates on the active sites of the metal (Cu and Mg). Therefore, the optimized ratio of metal Cu and Mg to Al-MCM-41 appears to be very important in order to achieve a high selectivity toward PDO production.[13] The ratio of 1 : 1 Cu and Mg on the support showed poorer performance among all bimetallic catalysts with a conversion of 70.7% and 26.1% 1,2-PDO production, followed by 59.5% glycerol conversion and 9.4% yield for 1,3-PDO. Cao *et al.*[57] synthesized a bifunctional catalyst (acidic and basic nature) using a Ni,Mg-based catalyst with 10%Ni/10%MgO/ZrO_2, which showed a glycerol conversion

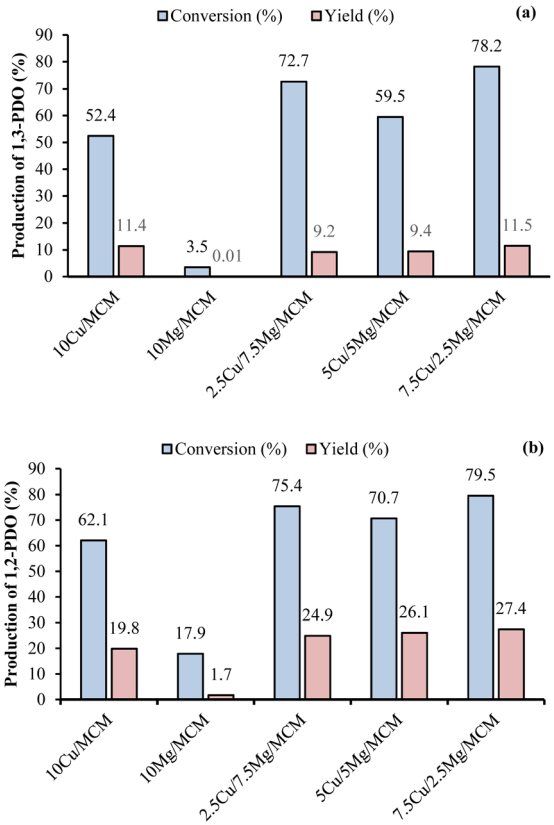

Fig. 9 Effect of using monometallic and bimetallic catalyst species, reaction conditions: (a) 220 °C, 4 h, 0.5 g of catalyst, 10 wt% of glycerol feedstocks in ethanol, 20 bar of N_2 (1,3-PDO); (b) 210 °C, 3 h, 0.5 g of catalyst, 10 wt% of glycerol feedstocks in ethanol, 5 bar of N_2 (1,2-PDO).

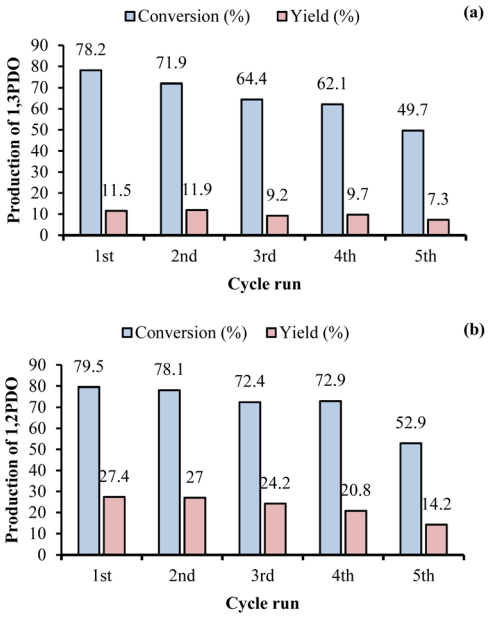

Fig. 10 Reusability test of bimetallic 7.5Cu/2.5Mg/MCM, reaction conditions: (a) 220 °C, 4 h, 0.5 g of bimetallic 7.5Cu/2.5Mg/MCM, 10 wt% of glycerol feedstocks in ethanol, 20 bar of N_2 (1,3-PDO); (b) 210 °C, 3 h, 0.5 g of bimetallic 7.5Cu/2.5Mg/MCM, 10 wt% of glycerol feedstocks in ethanol, 5 bar of N_2 (1,2-PDO).

of about 67.8% and 48.8% total selectivity. A research study performed by Chen *et al.*[58] also showed that the combination of the Ni–MgO alkaline catalyst exhibited superior activity for glycerol hydrogenolysis with about 67.8% conversion and 80.8% total selectivity of ethylene glycol, 1,2-propylene glycol and glycerol. Basic metal oxides, such as MgO and CuO, can be used as promoters on support by improving the thermal stability, enhancing the reversibility of the redox reactions suffered by the metal phase, and decreasing coke formation.[59]

Reusability test of bimetallic 7.5Cu/2.5Mg/MCM. The stability of the 7.5Cu/2.5Mg/MCM catalyst was verified by conducting a reusability study for up to five cycles, using the catalyst under optimum reaction conditions obtained from the previous parameter study. For every cycle use, the spent catalyst was washed with ethanol a few times to clean the impurities on the surface of the catalyst, followed by reduction treatment using a fixed-bed reactor with 25 mL min^{-1} flow of continuous hydrogen gas at 280 °C for 3 h. The obtained material was then utilized for the next tests or runs. Based on Fig. 10, a very high glycerol conversion (79.5%) and yield (27.4%) for 1,2-PDO production was obtained, and both values were found to slightly decline until the third cycle use. Both conversion and yield were found to be constant from the fourth cycle to the fifth cycle. Afterward, it decreased by 20% at the fifth cycle use. The conversion of glycerol and yield to 1,3-PDO was also elevated, which was 78.2% and 11.5%, respectively. It was found to gradually drop with a concurrent cycle use from the first to fifth cycles. As for the use of the catalyst after the first cycle, the conversion into other three-carbon products (such as ethylene glycol, ethanol and gas products) was found to slowly increase until the fifth cycle use. It was noticed that even after the 4th cycle, the glycerol conversion was still reasonable. A slight drop in the conversion and yield was observed, which was probably due to a small amount of metal leaching from the excessive washing of the catalysts.[60] Furthermore, traceable impurities from purified glycerol (such as inorganic salt, free fatty acid and soap) not only contribute to the low conversion of propanediols, it is one of the reasons for the declining performance of the catalyst. These impurities concentrate on the surface of the catalyst, clog the pores, and destabilize the catalyst performance over time.[61–63]

Product characterization

The HPLC chromatograms of the standard 1,2-PDO and 1,3-PDO indicate retention times at 12.4 and 12.6 min, respectively, as illustrated in Fig. 11. The chromatograms of the synthesized 1,2-PDO and 1,3-PDO at certain retention times were compared with those of standards to identify the target compounds, as both 1,2-PDO and 1,3-PDO possess almost identical chemical properties.

Fig. 12 displays the high-performance liquid chromatograms of the 1,2-PDO and 1,3-PDO utilizing the bimetallic Cu/Mg with 3 : 1 ratio on MCM, as it shows the highest yield compared to the other catalysts. The chromatogram showed the appearance of

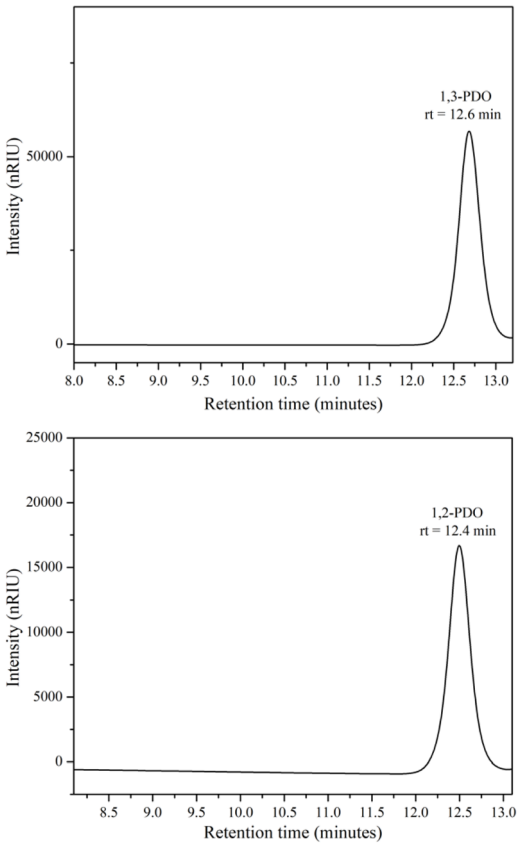

Fig. 11 HPLC chromatograms of standard 1,2-PDO and 1,3-PDO.

1,2-PDO peaks observed at the retention of 12.4 min. Meanwhile, 1,3-PDO peaks were detected at a retention time of 12.6 min, as shown in Fig. 11. However, the chromatogram also reveals the presence of three additional compounds with high intensity peaks at retention times of 9.7, 10.2 and 14.9 min, which were attributed to ethylene glycol, glycerol residue and ethanol, respectively. 1,2- and 1,3-PDO represented the most dominant peaks detected in the derived samples, followed by ethanol and ethylene glycol. Due to the C–C bond cleavage of glycerol or its intermediates, side products such as ethanol usually formed as the reaction used high temperatures to break down glycerol into smaller molecules such as acetol and hydroxyacetone, which can then be further reduced to form ethanol.[63] On the other hand, ethylene glycol can result from the rearrangement and hydrogenation of intermediates like glyceraldehyde or glycolaldehyde. These intermediates can form during the partial hydrogenolysis of glycerol, and may be reduced into ethylene glycol.[30]

The catalyst's pre-reaction and post-reaction physicochemical properties were compared to identify the structural integrity of the catalyst as the active sites on the catalyst's surface are exposed during the hydrogenolysis reaction to propanediols. The 7.5Cu/2.5Mg/MCM catalyst was used for up to five cycles at 220 °C for 4 h and 20 bar of N_2. The catalyst was treated for reusability studies, and the fifth cycle catalyst was used for further characterization using XRD and TEM analysis. Fig. 13 displays the pre-/post-reaction (a) XRD and (b) TEM analysis of 7.5Cu/2.5Mg/MCM after five cycles of use.

As discussed in the previous XRD results, Fig. 13(a) illustrates the Cu pattern with two distinct peaks of high intensity for the fresh catalyst at $2\theta = 35.5°$ and 38.7°, corresponding to the (002) and (111) planes, respectively. In contrast, the presence of the Mg species is confirmed by diffraction peaks

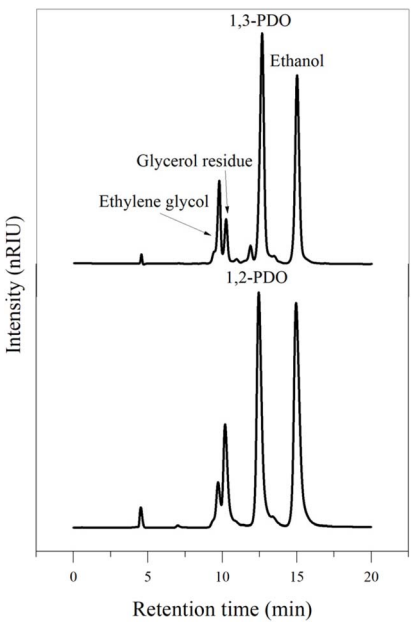

Fig. 12 HPLC chromatograms of 1,2-PDO and 1,3-PDO prepared using bimetallic 7.5Cu/2.5Mg/MCM as the catalyst.

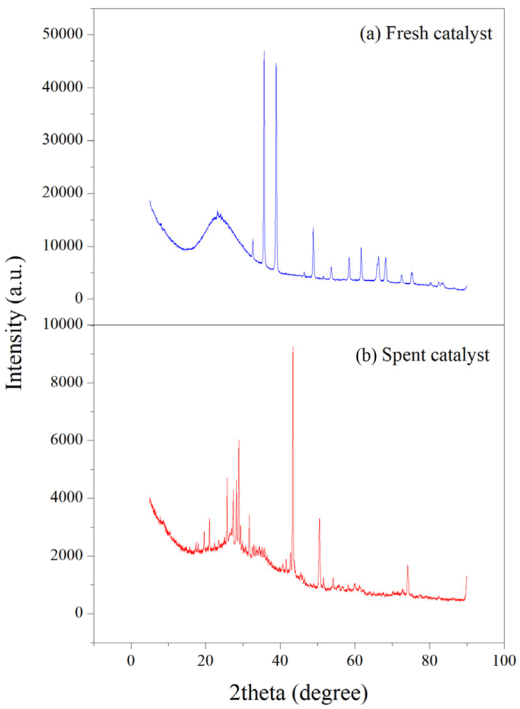

Fig. 13 XRD patterns of the (a) fresh and (b) spent 7.5Cu/2.5Mg/MCM catalysts after five cycles.

observed at $2\theta = 61.6°$ and 74.5°, which are assigned to the (220) and (311) planes, respectively. However, in Fig. 13(b) showing the spent catalyst, there are many impurity peaks detected at theta values around 20° to 30°. This can be explained by the formation of carbonaceous deposits (coke) or contaminants from feedstock, which often accumulate on the surface of the spent catalyst. These impurities contribute additional diffraction signals, further complicating the XRD pattern, which is in agreement with the studies done by Rosset & Perez-Lopez.[65]

As observed in Fig. 13(b), two sharp peaks of the CuO phase (which originated at $2\theta = 35.5°$ and 38.7°) were found to form a broad peak at 35.7°, whereas another peak was detected and shifted to a higher angle of 43.4°. The formation of the broad peak was due to the loss of long-range order, leading to peak broadening, shifting, or disappearance, while new peaks from amorphous or recrystallized phases emerged.[64] Meanwhile, another shifted sharp peak was attributed to the agglomeration of Cu nanoparticles due to lattice strain from metal sintering. Prolonged reaction leads to agglomeration of Cu nanoparticles, changing its crystallite size. These interactions were also found to alter the lattice parameters, causing peak shifts compared to the fresh catalyst.[65] For the MgO phase, the peaks originally observed at $2\theta = 61.6°$ and 74.5° (Fig. 13(a)) were found to shift to 50.4° and 74°, respectively. Carbon deposits block pores and alter the local chemistry, which can create microenvironments that favor metal dissolution. After many cycles of use, the support structure loses integrity, and metals anchored in pores or surface sites become more susceptible to leaching.[66] It is clear that the different intensities of the diffraction peaks indicate that there are structural changes between the crystal lattices.

Further characterization of the fresh and spent catalysts, up to five cycles of use, was carried out using TEM-EDX analysis to provide detailed insights into the catalyst's morphology and elemental distribution, as shown in Fig. 14. Transmission electron microscopy (TEM) analysis of the 7.5Cu/2.5Mg/MCM catalyst revealed distinct morphological differences between the fresh and spent samples. In the fresh catalyst, copper nanoparticles were observed to be finely dispersed in clusters form within the mesoporous channels of the MCM support, with particle sizes predominantly in the nanometer range. In contrast, the spent catalyst exhibited pronounced particle growth and agglomeration, consistent with sintering phenomena, as observed in Fig. 14(a) and (c). These changes explain the decline in catalytic activity after the second cycle of use. Moreover, darker contrast regions were observed in the spent catalyst compared to the fresh catalyst, suggesting carbon deposition (coke), which blocks and reduces the number of active sites.[67]

The morphological observations of the fresh and spent catalysts were further supported by EDX analysis of each elemental species, as shown in Fig. 15. Clear signals of Cu and Mg alongside Si and Al (from the zeolite framework) indicated

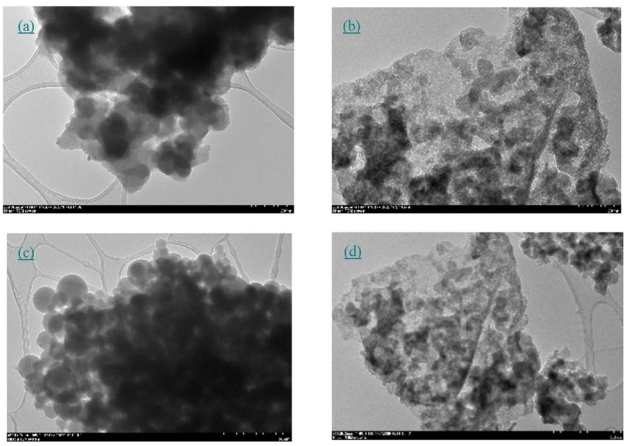

Fig. 14 TEM analysis on the (a, c) fresh and (b, d) spent 7.5Cu/2.5Mg/MCM catalysts.

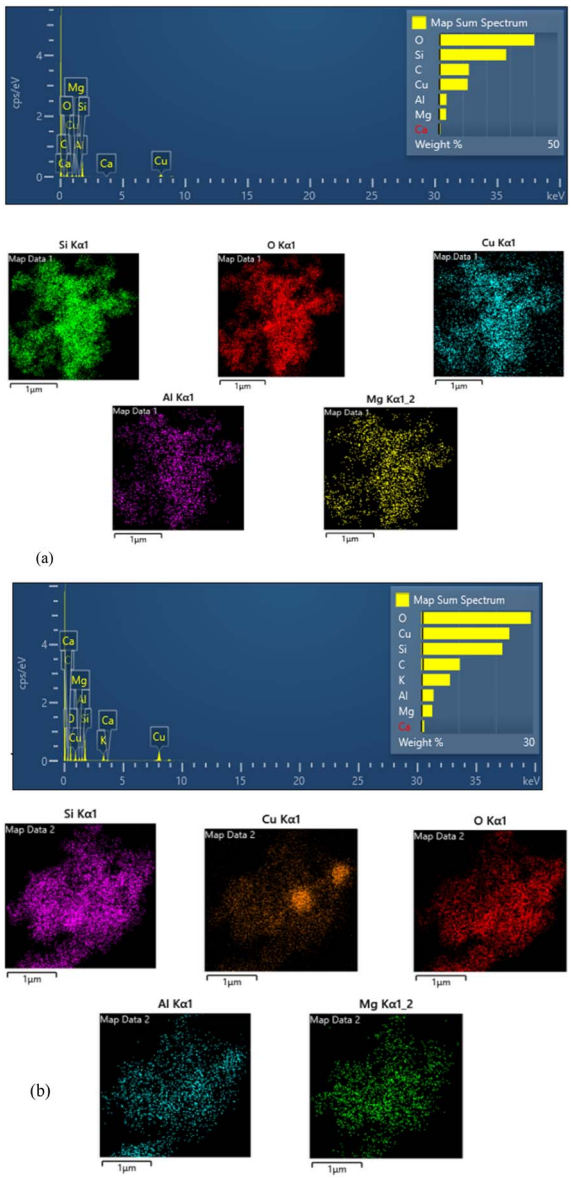

Fig. 15 EDX mapping of each element in the (a) fresh and (b) spent catalysts.

the homogeneous distribution of Cu and Mg incorporated into the zeolite matrix for the fresh 7.5Cu/2.5Mg/MCM catalyst. In contrast, a clear increment in Cu and Mg intensity within the support was observed for the spent catalyst. This was due to leaching or migration of Cu out of the active sites. Mg distribution may remain relatively stable, but Cu often shows clustering, as reported previously.[68] Moreover, increases in the intensity of the Cu species in the spent 7.5Cu/2.5Mg/MCM catalyst suggest pore blockage due to heavy coke deposition, which aligns with the TEM and XRD observations. The deviation of elemental ratios in the spent catalyst from the fresh state confirms the loss of active Cu and Mg species.

Conclusions

Glycerol was successfully converted into 1,2-propanediol and 1,3-propanediol through catalytic transfer hydrogenolysis without the use of external hydrogen gas. The experiments were conducted in a high-pressure batch reactor using Al-MCM-41, monometallic Cu/MCM with varying loadings, and bimetallic Cu/Mg/MCM with different ratios as catalysts. Among these, the 7.5Cu/2.5Mg/MCM catalyst demonstrated the highest glycerol conversion rate of 79.5%, along with a 1,2-PDO yield of 27.4%. The conversion and yield for 1,3-PDO were also enhanced, reaching 78.2% and 11.5%, respectively. Based on the reusability test conducted, it was found that the bimetallic 7.5Cu/2.5Mg/MCM retained its stable catalytic activity for up to three cycles; however, a gradual decline was observed during the fourth and fifth runs.

Author contributions

Conceptualization, A. R.; methodology, N.A.S.I.K.A.; software, N.A.S.I.K.A.; validation, A. R.; formal analysis, N.A.S.I.K.A.; investigation, N.A.S.I.K.A; resources, A. R.; data curation, N.A.S.I.K.A; writing—original draft preparation, N.A.S.I.K.A.; writing—review and editing, A. R.; visualization, A. R.; supervision, A. R.; project administration, A. R.; funding acquisition, A. R. All authors have read and agreed to the published version of the manuscript.

Conflicts of interest

There are no conflicts to declare.

Data availability

Data are contained within the article or supplementary information (SI). Supplementary information is available. See DOI: https://doi.org/10.1039/d5ra05648a.

Acknowledgements

The research was funded by Malaysian Ministry of Higher Education for Phase II HICOE CBBR (cost centre 015MA0-177) and Yayasan Universiti Teknologi PETRONAS: Pre-Commercialization Research Grant (YUTP-PRG, cost centre 015PBC-029). The authors thank Universiti Teknologi PETRONAS for providing the necessary facilities to support this project.

Notes and references

1 M. Balaraju, V. Rekha and P. S. Sai Prasad, *Catal. Lett.*, 2008, **126**, 119–124.
2 A. M. Ruppert, K. Weinberg and R. Palkovits, *Angew. Chem., Int. Ed.*, 2012, **51**, 2564–2601.
3 C. Montassier, J. Ménézo, L. Hoang, C. Renaud and J. Barbier, *J. Mol. Catal.*, 1991, **70**, 99–110.
4 D. K. Sohounloue, C. Montassier and J. Barbier, *React. Kinet. Catal. Lett.*, 1983, **22**, 391–397.
5 W. Zhou, J. Luo, Y. Wang, J. Liu, Y. Zhao, S. Wang and X. Ma, *Appl. Catal., B*, 2018, **242**, 410–421.
6 P. Sun, W. Zhang, X. Yu, J. Zhang, N. Xu, Z. Zhang, M. Liu, D. Zhang, G. Zhang, Z. Liu, C. Yang, W. Yan and X. Jin, *Front. Chem.*, 2022, **9**, 959414.
7 N. D. Kim, J. R. Park, D. S. Park, B. K. Kwak and J. Yi, *Chemistry*, 2012, **14**, 2638.
8 A. Corma, S. Iborra and A. Velty, *Chem. Rev.*, 2007, **107**, 2411–2502.
9 T. S. Ahmed, O. Y. Abdelaziz and G. W. Roberts, *Period. Polytech., Chem. Eng.*, 2017, **61**, 295–300.
10 V. G. Mendonça, I. C. Freitas, R. L. Manfro and M. M. Souza, *Appl. Catal., A*, 2022, **645**, 118838.
11 Y. Li, L. Ma, H. Liu and D. He, *Appl. Catal., A*, 2013, **469**, 45–51.
12 S. N. Delgado, D. Yap, L. Vivier and C. Especel, *J. Mol. Catal. A:Chem.*, 2012, **367**, 89–98.
13 S. S. Priya, V. P. Kumar, M. L. Kantam, S. K. Bhargava, A. Srikanth and K. V. R. Chary, *Ind. Eng. Chem. Res.*, 2015, **54**, 9104–9115.
14 S. S. Priya, P. Bhanuchander, V. P. Kumar, S. K. Bhargava and K. V. R. Chary, *Ind. Eng. Chem. Res.*, 2016, **55**, 4461–4472.
15 I. C. Freitas, R. L. Manfro and M. M. Souza, *Appl. Catal., B*, 2017, **220**, 31–41.
16 C. Wang, B. Dou, H. Chen, Y. Song, Y. Xu, X. Du, L. Zhang, T. Luo and C. Tan, *Int. J. Hydrogen Energy*, 2013, **38**, 3562–3571.
17 V. Yfanti and A. Lemonidou, *J. Catal.*, 2018, **368**, 98–111.
18 N. K. Mishra, P. Kumar, V. C. Srivastava and U. L. Stangar, *J. Environ. Chem. Eng.*, 2021, **9**, 105263.
19 C. H. Zhou, H. Zhao, D. S. Tong, L. M. Wu and W. H. Yu, *Catal. Rev.*, 2013, **55**, 369–453.
20 Z. Yuan, L. Wang, J. Wang, S. Xia, P. Chen, Z. Hou and X. Zheng, *Appl. Catal., B*, 2010, **101**, 431–440.
21 A. Martin, U. Armbruster, I. Gandarias and P. L. Arias, *Eur. J. Lipid Sci. Technol.*, 2012, **115**, 9–27.
22 M. R. Nanda, Z. Yuan, W. Qin, M. A. Poirier and X. Chunbao, *Austin Chem. Eng*, 2014, **1**, 1–7.
23 B. Dou, Q. Hu, J. Li, S. Qiao and Z. Hao, *J. Hazard. Mater.*, 2010, **186**, 1615–1624.
24 E. Westsson, S. Picken and G. Koper, *Chem. Commun.*, 2019, **55**, 1338–1341.
25 Z. I. Jibril, A. Ramli and K. Jumbri, *J. Jpn. Inst. Energy*, 2018, **97**, 200–204.

26 G. A. Eimer, L. B. Pierella and G. A. Monti, *Catal. Lett.*, 2002, **78**, 65–75.
27 S. Rahman, C. Santra, R. Kumar, J. Bahadur, A. Sultana, R. Schweins, D. Sen, S. Maity, S. Mazumdar and B. Chowdhury, *Appl. Catal., A*, 2014, **482**, 61–68.
28 A. Jankowska, A. Chłopek, A. Kowalczyk, M. Rutkowska, M. Michalik, S. Liu and L. Chmielarz, *Molecules*, 2020, **25**, 5651.
29 A. S. Al-Fatesh, R. Kumar, S. O. Kasim, A. A. Ibrahim, A. H. Fakeeha, A. E. Abasaeed, H. Atia, U. Armbruster, C. Kreyenschulte, H. Lund, S. Bartling, Y. A. Mohammed, Y. A. Albaqmaa, M. S. Lanre, M. L. Chaudhary, F. Almubaddel and B. Chowdhury, *Ind. Eng. Chem. Res.*, 2021, **61**, 164–174.
30 B. Mallesham, P. Sudarsanam, B. V. S. Reddy and B. M. Reddy, *Appl. Catal., B*, 2015, **181**, 47–57.
31 A. Jankowska, A. Kowalczyk, M. Rutkowska, M. Michalik and L. Chmielarz, *Molecules*, 2021, **26**, 1807.
32 G. Busca, L. Lietti, G. Ramis and F. Berti, *Appl. Catal., B*, 1998, **18**, 1–36.
33 A. Ungureanu, B. Dragoi, A. Chirieac, C. Ciotonea, S. Royer, D. Duprez, A. S. Mamede and E. Dumitriu, *ACS Appl. Mater. Interfaces*, 2013, **5**, 3010–3025.
34 Y. S. Yun, D. S. Park and J. Yi, *Catal. Sci. Technol.*, 2014, **4**, 3191–3202.
35 J. Y. Kim, J. A. Rodriguez, J. C. Hanson, A. I. Frenkel and P. L. Lee, *J. Am. Chem. Soc.*, 2003, **125**, 10684–10692.
36 A. M. Bruno, T. D. R. Simões, M. M. V. M. Souza and R. L. Manfro, *RSC Adv.*, 2020, **10**, 31123–31138.
37 S. Mondal, A. A. Arifa and P. Biswas, *Catal. Lett.*, 2017, **147**, 2783–2798.
38 K. Shun, K. Mori, S. Masuda, N. Hashimoto, Y. Hinuma, H. Kobayashi, H. Yamashita, K. Shun, K. Mori, S. Masuda, N. Hashimoto, Y. Hinuma, H. Kobayashi and H. Yamashita, *Chem. Sci.*, 2022, **27**, 8137–8147.
39 C. Gao, J. Huang, P. Zhang, X. Jiang and Z. You, *Transition Met. Chem.*, 2025, **6**, 1033–1041.
40 M. Selvaraj, A. Pandurangan, K. Seshadri, P. Sinha and K. Lal, *Appl. Catal., A*, 2003, **242**, 347–364.
41 F. Guo, S. Guo, X. Wei, X. Wang, H. Xiang, Z. Qiu and L. Zhao, *Catal. Lett.*, 2014, **144**, 1584–1593.
42 A. Sakthivel, S. Dapurkar, N. Gupta, S. Kulshreshtha and P. Selvam, *Microporous Mesoporous Mater.*, 2003, **65**, 177–187.
43 A. Święs, A. Kowalczyk, M. Rutkowska, U. Díaz, A. E. Palomares and L. Chmielarz, *Catalysts*, 2020, **10**, 734.
44 V. García, J. J. Fernández, W. Ruíz, F. Mondragón and A. Moreno, *Catal. Commun.*, 2009, **11**, 240–246.
45 A. Vinu, K. Ariga, S. Saravanamurugan, M. Hartmann and V. Murugesan, *Microporous Mesoporous Mater.*, 2004, **76**, 91–98.
46 M. Marosz, B. Samojeden, A. Kowalczyk, M. Rutkowska, M. Motak, U. M. Diaz, A. E. Palomares and L. Chmielarz, *Materials*, 2020, **13**, 2399.
47 J. Chen, Q. Xia, Y. Wang and Y. Huang, *Front. Chem. Eng.*, 2020, **2**, 3.
48 N. Azri, I. Ramli, U. I. Nda-Umar, M. R. Shamsuddin, M. I. Saiman and Y. H. Taufiq-Yap, *J. Taiwan Inst. Chem. Eng.*, 2020, **112**, 34–51.
49 L. Zheng, S. Xia and Z. Hou, *Appl. Clay Sci.*, 2015, **118**, 68–73.
50 A. Ghorbani and A. K. Dalai, *RSC Adv.*, 2026, **5**, 4252–4274.
51 Q. Tong, A. Zong, W. Gong, L. Yu and Y. Fan, *RSC Adv.*, 2016, **89**, 86663–86672.
52 Y. Amada, Y. Shinmi, S. Koso, T. Kubota, Y. Nakagawa and K. Tomishige, *Appl. Catal., B*, 2011, **105**, 117–127.
53 F. Chang, H. Yang, L. S. Roselin and W. Kuo, *Appl. Catal., A*, 2006, **304**, 30–39.
54 G. Carotenuto, R. Tesser, M. Di Serio and E. Santacesaria, *Catal. Today*, 2012, **203**, 202–210.
55 F. Mauriello, A. Vinci, C. Espro, B. Gumina, M. G. Musolino and R. Pietropaolo, *Catal. Sci. Technol.*, 2015, **5**, 4466–4473.
56 A. Ramesh, B. M. Ali, R. Manigandan, C. T. Da and M. Nguyen-Le, *Mol. Catal.*, 2022, **525**, 112358.
57 X. Cao, Q. Zhang, D. Jiang, Q. Liu, L. Ma, T. Wang and D. Li, *Chin. J. Chem. Phys.*, 2015, **28**, 338–344.
58 X. Chen, X. Wang, S. Yao and X. Mu, *Catal. Commun.*, 2013, **39**, 86–89.
59 J. P. Da SQ Menezes, A. P. D. S. Dias, M. A. Da Silva and M. M. Souza, *Int. J. Hydrogen Energy*, 2020, **45**, 22906–22920.
60 C. Fan, H. Guan, H. Zhang, J. Wang, S. Wang and X. Wang, *Biomass Bioenergy*, 2011, **35**, 2659–2665.
61 D. Samul, K. Leja and W. Grajek, *Ann. Microbiol.*, 2014, **64**, 891–898.
62 D. A. Boga, F. Liu, P. C. A. Bruijnincx and B. M. Weckhuysen, *Catal. Sci. Technol.*, 2015, **6**, 134–143.
63 N. Vera-Hincapie, U. Iriarte-Velasco, J. Ayastuy and M. Gutiérrez-Ortiz, *J. Environ. Chem. Eng.*, 2024, **12**, 112357.
64 M. Rosset and O. W. Perez-Lopez, *React. Kinet., Mech. Catal.*, 2017, **123**, 689–705.
65 S. Liu, Y. Hu, Q. Zhang, X. Tan, H. Cui, F. Li, H. Lei and O. Zhuo, *Catalysts*, 2025, **15**, 546.
66 T. Xie, X. Li, H. Sun and Z. Dan, *Environ. Sci. Pollut. Res.*, 2022, **29**, 63393–63406.
67 X. Tang, J. Ye, L. Guo, T. Pu, L. Cheng, X. Cao, Y. Guo, L. Wang, Y. Guo, W. Zhan and S. Dai, *Adv. Mater.*, 2023, **35**, 2208504.
68 S. Sakane, K. Akimoto, K. Konishi, K. Takaoka, H. Iwatsuki, M. Akutsu, T. Sugai and H. Tanaka, *ACS Omega*, 2023, **9**, 970–976.